Image-driven constitutive modelling of myocardial fibrosis

Vicky Y. Wang[1], Justyna A. Niestrawska[2], Alexander J. Wilson[1,3], Gregory B. Sands[1,3], Alistair A. Young[1,4], Ian J. LeGrice[1,3], Martyn P. Nash[1,5]

[1]*Auckland Bioengineering Institute, University of Auckland, New Zealand*

[2]*Institute of Biomechanics, Graz University of Technology, Graz, Austria*

[3]*Department of Physiology, University of Auckland, New Zealand*

[4]*Department of Anatomy with Radiology, University of Auckland, New Zealand*

[5]*Department of Engineering Science, University of Auckland, New Zealand*

Abstract

Myocardial fibrosis is a pathological process that occurs during heart failure. It involves microstructural remodelling of normal myocardial tissue, and consequent changes in both cardiac geometry and function. The role of myocardial structural remodelling in the progression of heart failure remains poorly understood. We propose a constitutive modelling framework, informed by high-resolution images of cardiac tissue structure, to model the mechanical response of normal and fibrotic myocardium. This image-driven constitutive modelling approach allows us to better reproduce and understand the relationship between structural and functional remodelling of ventricular myocardium during heart failure.

Keywords: Myocardial fibrosis, diastolic heart failure, confocal imaging, finite element modelling, constitutive properties

1 Introduction

The heart is a four-chambered muscular organ that acts as a cyclic mechanical pump to circulate blood throughout the body. Heart failure (HF) is associated with a reduced ability to fill and/or eject blood. HF may involve the right and/or left ventricle, though left ventricular (LV) dysfunction is more common. Two types of syndromes, diastolic HF (DHF) and systolic HF (SHF), have been defined based on whether cardiac filling or ejection is impaired, though often HF involves a combination of diastolic and systolic dysfunction. The diagnosis and treatment options for SHF are better described than DHF [1], however, the mechanisms accounting for ventricular dysfunction and the link between the different forms of HF are poorly understood.

Structural remodelling of the LV has been identified as one of the key mechanisms underpinning the development of ventricular dysfunction in HF [1, 2]. Remodelling can be initiated by changes in physiological, geometrical and/or haemodynamic loading conditions, and eventually leads to global changes in ventricular geometry, regional wall thickening or thinning (manifested by myocyte growth, parallel or serial addition of myocytes), and alteration of myocardial constituents (myocardial fibrosis) [3]. Fibrosis is the accumulation of excessive fibrous tissue in the interstitial space, and is a common consequence of many pathological processes involving failure of organs such as the kidney, liver or heart [4-6]. The remodelling process can result in altered global properties of the ventricular chamber (e.g. elevation of chamber stiffness [7, 8]) or of local myocardial tissue properties, both of which are important determinants of the mechanical performance of the heart.

Over the past decade, several studies [7-10] have investigated the extent of myocardial fibrosis in HF using animal models. One of the most studied animal models is the spontaneously hypertensive rat (SHR). In comparison to the Wistar-Kyoto rat (WKY) controls, the SHR naturally develops

hypertension early in life, leading to premature death from HF at around 2 years. The structural changes observed in hearts of these animals closely resemble those of human HF [7, 9, 11, 12]. *Ex vivo* histological imaging of both rat and human tissues has revealed that myocardial fibrosis manifests as diffuse scarring [7] and proliferation of collagen, with endomysial collagen encasing the myocytes [12], and perimysial collagen infiltrating the cleavage planes [8, 12].

In the SHR, LV diastolic dysfunction is demonstrated by elevated chamber stiffness as derived from the *ex vivo* LV pressure–volume curves [8], and the *ex vivo* stress–strain relationship of cardiac trabeculae [7]. Based on these observations, interstitial fibrosis was thought to be the key cause of LV chamber stiffening [5, 7, 8]. It has been hypothesised that ventricular hypertrophy, due to the parallel addition of cardiac myocytes, cannot solely account for the observed diastolic dysfunction [5], however this has not been supported by convincing mechanistic evidence. Recently, *in vivo* investigation of human failing hearts has been made possible by obtaining myocardial T1 maps using cardiac magnetic resonance imaging. Pre- and post-contrast T1 can be used to calculate extra-cellular volume, in which increase is linked with myocardial fibrosis. Myocardial fibrosis has been found to be correlated with decreased systolic circumferential wall strain and impaired ventricular diastolic function [13, 14]. Despite extensive research on localising myocardial fibrosis during HF, the fundamental biomechanical effects of myocardial tissue remodelling are still unknown. In addition, the relative contributions of each of the remodelling factors to diastolic dysfunction are yet to be quantified.

Because of the complex relationship between structural remodelling and mechanical dysfunction, understanding of cardiac mechanics in health and disease will only be gained through mathematical modelling. Over the past two decades, advancement in cardiac imaging techniques has enabled myocardial mechanics modelling studies to evolve substantially from generic to subject-specific analyses. By constructing mathematical models of the LV that integrate anatomically-accurate

geometry, microstructure, and reliable myocardial constitutive properties, one can perform forward mechanics analyses to examine the effects of structural remodelling on mechanical function [15, 16]. With *in vivo* structural and functional information now attainable, it is also feasible to estimate constitutive properties under diseased conditions [17-19]. However, the estimated mechanical properties of myocardium have not been directly related to the underlying structural changes, and there is no standard systematic approach to characterise the constitutive properties of fibrotic myocardium.

In this study, we have developed an image-based constitutive modelling framework to differentiate the roles of shape change, microstructural tissue remodelling, and changes in the passive mechanical response during DHF. We addressed the following specific research questions:

1) Can geometric remodelling alone account for the increase in chamber stiffness in diseased SHR hearts?
2) Can myocardial fibrosis together with geometric remodelling explain the increase in chamber stiffness in diseased SHR hearts?

By incorporating indices of microstructural remodelling directly into the constitutive equation, and tuning the unknown material parameters using *ex vivo* LV cavity compliance curves for normal (WKY) and diseased (SHR) hearts exhibiting DHF, we have found that changes in LV geometry and proliferation of endomysial and perimysial collagen can account for the changes observed in the pressure-volume relationship, and hence compliance, of the LV chamber.

2 Constitutive modelling of myocardial tissue

The mechanical response of healthy myocardium is orthotropic due to its 3D laminar microstructural arrangement. Detailed *ex vivo* confocal imaging has shown that myocardium is primarily made of sheetlets of myocytes, which are typically around three or four cells thick, and interconnected by a dense network of collagen [20, 21] (Figure 1 (a)). Two components of the collagen hierarchy in myocardium (Figure 1 (b)) have been found to play important roles in modulating the complicated myocardial motion throughout the cardiac cycle. Endomysial collagen surrounds individual myocytes, while perimysial collagen surrounds, and interconnects, the surfaces of neighbouring sheetlets [22]. Material orthotropy can be represented by a set of orthogonal axes (Figure 1 (a)) consisting of the fiber axis (*f*), the sheet axis (*s*) perpendicular to the fiber axis but within the sheetlet plane, and the sheet-normal axis (*n*) defined to be perpendicular to the plane of the sheetlet (defined by *f* and *s*).

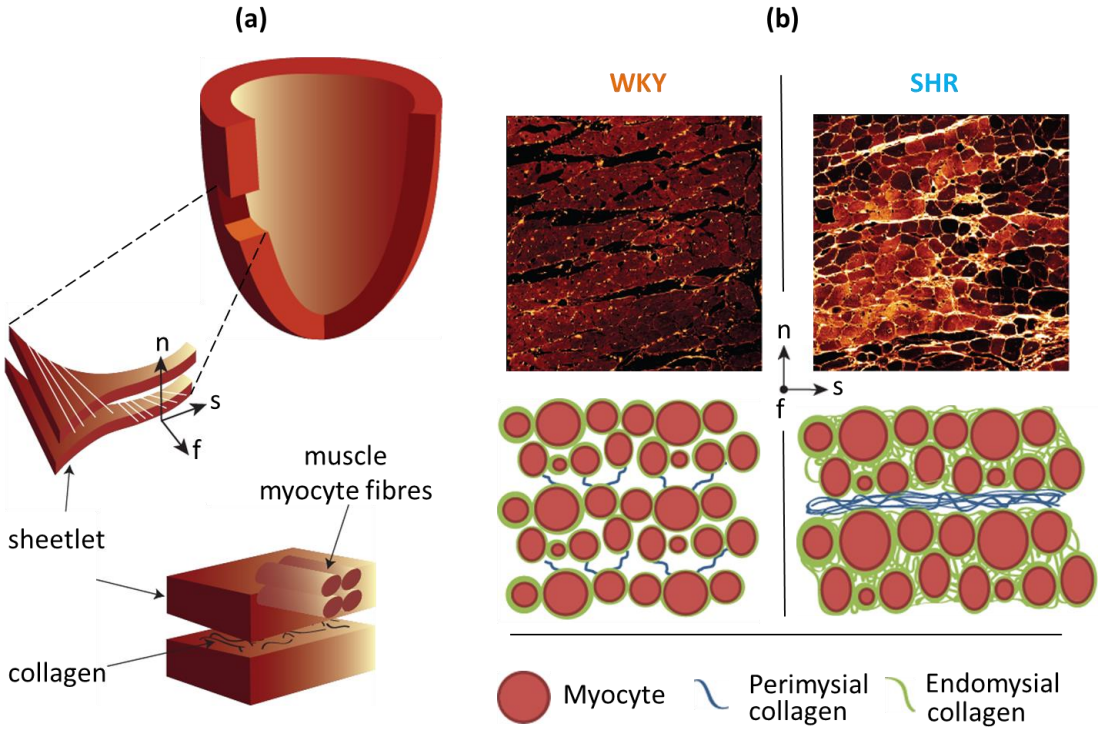

Figure 1: (a) Schematic showing the laminar arrangement of myocyte fibres from which the orthotropic material axes are defined (adapted from [20]). (b) Top left: high resolution *ex vivo* confocal images of a tissue block excised from a 12-month old WKY rat heart demonstrating the presence of collagen (brighter intensity) and cleavage planes (black gaps). Top right: high

resolution *ex vivo* confocal images of a tissue block excised from a SHR heart at 12 months. Bottom left: WKY schematic showing the 3D organisation of myocyte fibres in cross-section (brown), perimysial collagen (blue) and endomysial collagen (green). Bottom right: SHR schematic showing the proliferation of perimysial collagen filling in the cleavage space, and increased endomysial collagen around myocytes .

2.1 Structural and functional remodelling of fibrotic myocardium

A previous study by our group [8] assembled high-resolution images of the microstructure of WKY and SHR hearts using extended-volume confocal microscopy. In comparison to the control WKY hearts, there was evidence of substantial reorganisation of the laminar structure (i.e. fusion of sheetlets of myocytes whereby cleavage space was filled with perimysial collagen) and increased amounts of endomysial collagen surrounding myocytes in the SHRs (see Figure 1 (b)). Differences in the global passive mechanical function were investigated by recording passive *ex vivo* pressure-volume measurements from isolated hearts and deriving the relationships between LV compliance (characterised using the slope of the pressure-volume curve) and LV filling pressure (Figure 2). Comparing the LV compliance curves between the WKY and SHR hearts (Figure 2) revealed strikingly different chamber compliances over the physiological range of pressures (i.e. < 15 mmHg), however these differences were minimal once LV filling pressures exceeded 15 mmHg.

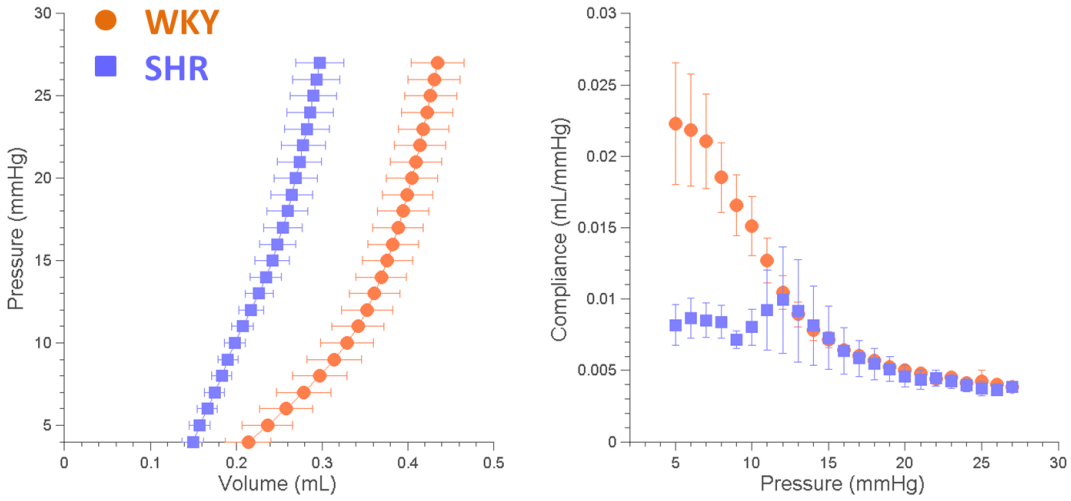

Figure 2: Average (mean ± SD) passive LV pressure-volume (left) and LV compliance (right) data for WKY hearts (orange circles; n = 9) and SHR hearts (blue squares; n = 10) at the age of 12 months (adapted from [8]).

It is difficult to understand the mechanistic link between collagen proliferation at the microscopic level and stiffening of the LV chamber at the organ level without using a computational modelling approach. To reliably represent LV mechanics for diseased myocardium, it is important to choose an appropriate constitutive equation.

2.2 Passive constitutive models

Several studies have proposed hyperelastic constitutive equations (i.e. neglecting viscous effects) to model the orthotropic properties of normal myocardium. Frequently cited constitutive models include the Fung-type single exponential strain energy density function [23], the pole-zero strain limiting function [24], and a separated Fung-type exponential strain energy density function [25, 26]. All of these models were motivated by the orthotropic nature of material structure and

behaviour, and have been shown to reproduce experimental data from biaxial testing [27] and simple shear test of tissue blocks [28]. These constitutive equations have also been integrated into finite element (FE) models of *in vivo* cardiac mechanics to parameterise *in vivo* material properties, which cannot be measured in the intact heart.

While the above constitutive models can account for orthotropic material behaviour, applications of these models have been limited to the study of healthy myocardium. The constitutive equations are generally not applicable for analysing the mechanical behaviour of fibrotic tissue for the following reasons:

- **Parameters lack physical meaning**: Given that many myocardial constitutive models have been empirically derived based on functional data, as opposed to the biophysical properties of myocardium, the material parameters typically lack physiological meaning. Significant research progress has been made on the development of microstructural based constitutive models for collagenous tissues. This style of constitutive modelling can account the angular distributions of fibres [29], fibre splay, and collagen crimp [30, 31]. Although these studies have shown that incorporating microstructural characteristics is essential for modelling the mechanical behaviour of collagen fibrils, the suitability of these models to study myocardium remains unknown due to the lack of the quantifications of these microstructural indices.
- **Parameter correlation**: The parameters used in these models are often co-dependent, which can make parameter identification difficult. This issue is more profound in the single-term exponential function [23] due to the inability to separate the mechanical response along each of the material axes. Modifications have been made by defining a separate term for each of the microstructural material axes (*f*,*s*,*n*) [24-26].
- **Parameter identifiability**: The correlation between material constants can lead to numerical instabilities during parameter estimation, resulting in poor parameter identifiability. In such

cases, similar mechanical behaviour can result from different combinations of material parameters.

These shortcomings add complexity and uncertainty to the interpretation of the fitted material parameters.

3 An image-driven constitutive model

For this study, we aimed to construct a constitutive modelling framework that incorporated structural parameters informed by high-resolution *ex vivo* microstructural data in order to gain an understanding of the biomechanical consequences of myocardial fibrosis at the continuum level. This framework was applied to examine the relative roles of geometric remodelling and collagen proliferation during DHF using geometric models fitted to 3D *in vivo* cardiac magnetic resonance images (MRI) and *ex vivo* compliance data of isolated hearts.

3.1 Constitutive model development

3.1.1 Normal myocardium

In our modelling framework, we adapted the Holzapfel-Ogden constitutive equation [26] as it not only successfully reproduces the complex shearing mechanical behaviour reported in Dokos et al. [28], but it also satisfies the convexity conditions, which provide material stability and physically meaningful predictions of mechanical behaviour. The original Holzapfel-Ogden constitutive equation includes four strain invariants (I_1, I_{4f}, I_{4s}, I_{4fs}) to represent mechanical response in the non-muscular matrix, fibre axis, sheet axis, and fibre-sheet plane, respectively. The isotropic (first) term in the original formulation combined behaviour along all three microstructural axes, and therefore did not allow the mechanical response in each of the material directions to be independently controlled. In order to decouple the response along these axes, an approximately equivalent

formulation was constructed by omitting the isotropic term from the original formulation and adding an exponential term describing the sheet-normal direction response (Eq. 1).

$$\bar{W} = \frac{a_f}{2b_f}\left\{\exp\left[b_f\left(I_{4f}-1\right)^2\right]-1\right\} + \frac{a_s}{2b_s}\{\exp[b_s(I_{4s}-1)^2]-1\} + \frac{a_n}{2b_n}\{\exp[b_n(I_{4n}-1)^2]-1\} + \frac{a_{fs}}{2b_{fs}}\left\{\exp\left[b_{fs}I_{8fs}^2\right]-1\right\} \quad (1)$$

where $I_{4f} = \boldsymbol{f}\cdot(\boldsymbol{Cf})$; $I_{4s} = \boldsymbol{s}\cdot(\boldsymbol{Cs})$; $I_{4n} = \boldsymbol{n}\cdot(\boldsymbol{Cn})$; $I_{4fs} = \boldsymbol{f}\cdot(\boldsymbol{Cs})$

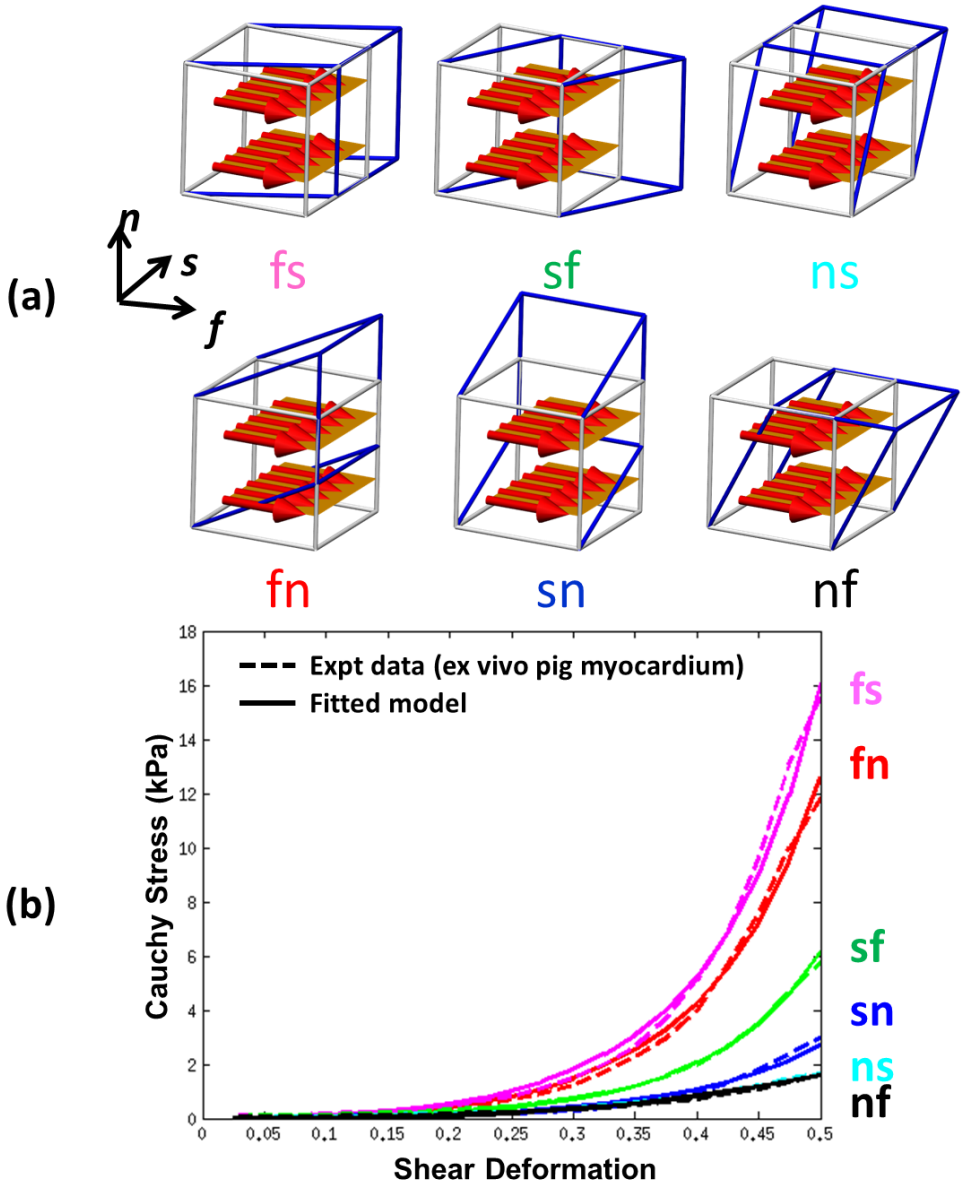

Figure 3: (a) Undeformed cubes (silver) embedded with sheetlets (gold planes) of fibres (red arrows) and deformed (blue) cubes for six modes of shear deformation. (b) Experimental data on

the relationship between the Cauchy stress and the amount of shear deformation (dashed lines) (adapted from [28]) superimposed with the model predicted curves (solid lines) based on the fitted material parameters.

The material response along each of the microstructural axes only plays a role in the overall mechanical response when their associated invariants (I_{4f}, I_{4s} and I_{4n}) are larger than 1 (i.e. undergoing stretch). To parameterise this reformulation (Eq. 1), we fitted the material constants (a_f, a_s, a_n, a_{fs}, b_f, b_s, b_n, and b_{fs}) to *ex vivo* experimental data describing simple shear of pig myocardial tissue blocks [28]. This set of experimental data was chosen to tune the eight material constants, because they included stress-strain curves in multiple modes of shear deformation. Compared to biaxial stretch experiments, these data provide much richer information on tissue deformation. To simulate the simple shear experiments, single-element linear Lagrange FE models of the tissue cubes were generated based on the size (3 mm x 3 mm x 3 mm) and microstructural arrangement of the tissue blocks (Figure 3 (a)). We then simulated six modes of shear deformation using in-house FE analysis software package *CMISS* [1]. Displacement boundary constraints (50% of shear displacement) were applied onto the appropriate surface using the same number of steps as the experiments (i.e. 20 steps). For each mode of shear deformation, we predicted Cauchy shear stresses at each of the displacement steps, resulting in 120 stress estimates in total. Finally, the material parameters were optimised using the MATLAB built-in optimiser *lsqnonlin*[2] to provide the best match between the model-predicted shear stresses and the stresses calculated from experimental recordings. To illustrate the goodness-of-fit, both the model-predicted and the experimental stress-displacement curves for all modes of deformation are provided in Figure 3 (b). Optimisations were performed starting from several different sets of initial parameter estimates to help avoid problems

[1] www.cmiss.org.
[2] The MathWorks, Inc., Natick, Massachusetts, United States.

associated with any local minima of the objective function. The optimal parameters are listed in Table 1.

Table 1: Material parameters for the constitutive equation (Eq. 1) proposed in this study, estimated to best match the simple shear experimental data reported in Dokos et al. [28] the constitutive equation (Eq. 1) proposed in this study.

a_f (kPa)	a_s (kPa)	a_n (kPa)	a_{fs} (kPa)	b_f	b_s	b_n	b_{fs}
24.8	7.0	6.4	0.4	11.3	7.1	0.2	11.7

3.1.2 Fibrotic myocardium

To model the mechanical properties of fibrotic myocardium (as shown in Figure 1), we introduced parameters into the constitutive equation that directly reflect collagen proliferation (Eq. 1), which could provide a biophysical and structural basis for explaining its effect on chamber function. LeGrice et al. [8] quantified and compared the changes in endomysial and perimysial collagen fractions for a group of WKY rats and SHRs at 12 months, the age at which SHRs are known to exhibit stiffening of the myocardial chamber compared to the WKY hearts. While the total collagen fraction (0.11 for WKY versus 0.16 for SHR) and endomysial collagen fraction (0.025 for WKY versus 0.1 for SHR) were significantly elevated compared to the WKY rats, there was no significant difference between the perimysial collagen fractions for the normal and diseased hearts (0.06 for WKY versus 0.054 for SHR). This lack of change in perimysial collagen appeared to be inconsistent with changes indicated by the structural images (Figure 1 (b) bottom left). This inconsistency was attributed to the fact that the myocytes had hypertrophied at 12-months and the reorganisation of perimysial collagen appears to give rise to a lower density estimate. Thus, collagen volume fraction evaluated from the confocal images does not accurately reflect the remodelling of perimysial collagen, and is therefore not an appropriate parameter to be used in the

constitutive equation to describe myocardial stiffening and the associated differences in chamber compliance.

The confocal images indicated that both perimysial and endomysial collagen strands are thickened in fibrosis (Figure 1 (b)). Based on these observations, we proposed to modify the constitutive equation (Eq. 1) by modulating the stiffnesses along the fibre and sheet axes by the degree of endomysial collagen thickening (t_{endo}) to represent the likely constraining effect of this structural remodelling on the mechanical response in the plane of the sheetlet. In addition, the degree of perimysial collagen thickening (t_{peri}) was used to modulate the stiffness properties in the sheet-normal direction to represent the likely effect of the observed sheet fusion on tissue mechanics. Both parameters were determined directly from the high resolution confocal microscopy images prior to mechanics analysis. The modified constitutive model is given in Eq. 2. A number of plausible alternative formulations were considered (see Appendix 1), but this model was selected as it provided the best fit to the experimental data as discussed later.

$$\bar{W} = \frac{\boldsymbol{t_{endo}} a_f}{2b_f}\left\{\exp\left[b_f\left(I_{4f}-1\right)^2\right]-1\right\} + \frac{\boldsymbol{t_{endo}} a_s}{2b_s}\{\exp[b_s(I_{4s}-1)^2]-1\} + \frac{\boldsymbol{t_{peri}} a_n}{2b_n}\{\exp[b_n(I_{4n}-1)^2]-1\} + \frac{a_{fs}}{2b_{fs}}\left\{\exp\left[b_{fs}I_{8fs}^2\right]-1\right\} \quad (2)$$

3.2 Simultaneous estimation of passive constitutive properties of normal and fibrotic tissue

To assess the suitability of the modified constitutive equation (Eq. 2) for modelling the normal (WKY) and failing (SHR) hearts, we integrated the constitutive equation into an inverse FE mechanics modelling framework to model the *ex vivo* compliance-pressure curves reported in [8] because subject-specific measurements were unavailable for the rat hearts studied here. Firstly, we

constructed subject-specific LV FE models (customised from a single-element axisymmetric prolate-spheroidal model) based on the endocardial and epicardial surface information derived from 3D *in vivo* cardiac MR images of two WKY and two SHR hearts (Figure 4 (a) & (b)) via guide-point modelling [32]. Secondly, *in vivo* measurements of fibre and sheetlet orientations were not available for these hearts, therefore, we prescribed a fibre field according to histological measurements [33, 34] with helix angles varying from -60 ° at the epicardium to +70 ° at the endocardium, and a homogeneously distributed sheet angle of 30 ° (Figure 4 (c)). Thirdly, we simulated the *ex vivo* passive inflation experiment by applying pressure to the endocardial surfaces of the FE models from 0 mmHg to a maximum filling pressure of 15 mmHg at 1 mmHg intervals in accordance with the experiments reported in [8] . From the model-predicted passive pressure-volume curves, we derived LV chamber compliance curves by calculating the inverse of the instantaneous gradient. An objective function, representing the combined differences between the model-predicted and experimentally measured compliance-pressure curves for all study cases (2 WKY and 2 SHR hearts), was constructed (Eq. 3). Given that the experimental compliance-pressure curves presented in [8] only reported the mean ± SD for groups of WKY and SHR hearts, we assumed that the two WKY cases studied here exhibited the same compliance behaviour as the group-averaged WKY rats in [8], and similarly the two SHR cases exhibited the same compliance behaviour as the group-averaged SHR. It is worthwhile noting that the material constants listed in Table 1 could not be readily applied as the parameters were tuned to the data from *ex vivo* pig hearts as opposed to rat hearts. Consequently, material parameters were re-estimated by minimising the objective function described in Eq. 3.

$$\Omega = \sqrt{\frac{\sum_1^N \left(LVC_{N,model} - LVC_{N,experiment}\right)^2}{N}} \tag{3}$$

where N = 44 (11 data points per case) and LVC represents LV compliance.

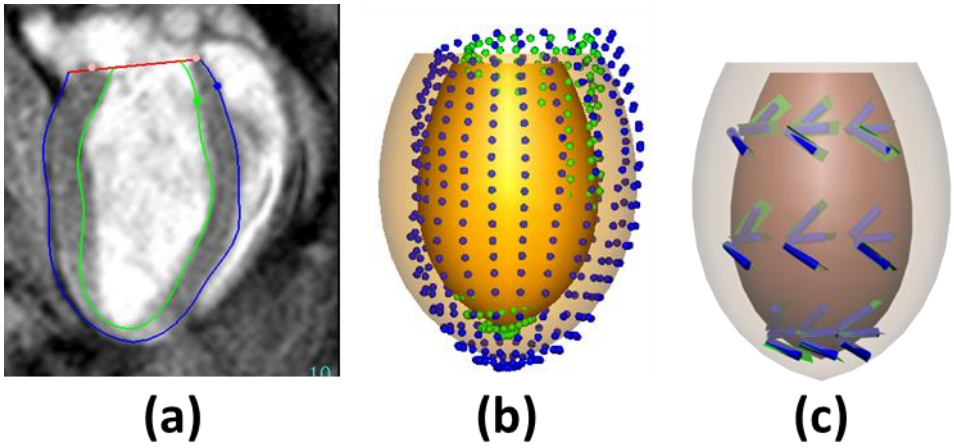

Figure 4: (a) *In vivo* cardiac MRI of a normal (WKY) rat heart superimposed with endocardial (green) and epicardial (blue) boundaries of the LV guide-point model. (b) Endocardial and epicardial surface data clouds overlaid with a LV FE model. (c) LV FE model superimposed with assumed fibre (blue cylinders) and sheet (green plane) angles.

4 Results

We applied the inverse modelling approach to two normal (WKY) hearts and two DHF (SHR) hearts to examine the hypotheses introduced in section 1. Results for each hypothesis are presented below.

4.1 Hypothesis 1: LV shape changes explain the decreased compliance

The LV models built from the 3D *in vivo* cardiac MR images of the four hearts (Figure 5) showed that the two diseased hearts (SHR) had significantly larger LV masses, moderately elevated LV end-diastolic volumes (EDV), and lower LV ejection fractions (EF), compared to the control (WKY) hearts (Table 2). The larger LV mass indicated substantial LV hypertrophy, and the concurrent increase in EDV suggested the nature of the hypertrophy may be eccentric. Given that the pumping ability (e.g. EF) of the diseased hearts was only affected by approximately 7 %, it seems likely that the SHRs were only suffering from diastolic dysfunction.

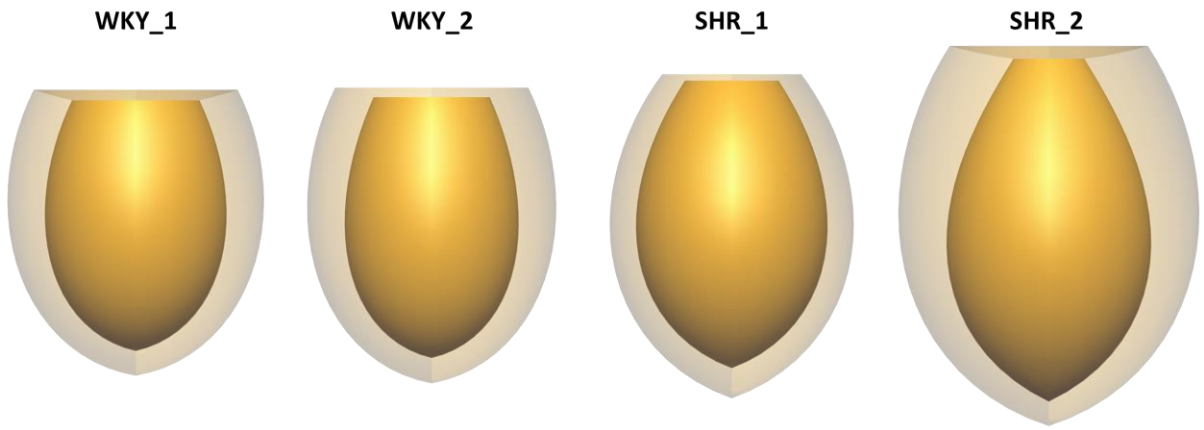

Figure 5: 3D LV FE models customised to *in vivo* MRI of two WKY and two SHR hearts at diastasis.

Table 2: Summary of LV geometric and functional measurements of two normal (WKY) and two diseased (SHR) hearts. (EDV: end-diastolic volume; EF: ejection fraction)

Animal Type	**LV Mass (mg)**	**EDV (µl)**	**EF (%)**
WKY_1	797	932	59
WKY_2	800	877	63
SHR_1	643	876	52
SHR_2	1575	1575	56

To address hypothesis 1, we used the constitutive equation in Eq. 1 to test whether the decreased LV compliance for the diseased hearts could be explained by just the observed changes in LV shape. In this analysis, a single set of material constants were simultaneously fitted to best match the *ex vivo* LV compliance curves of normal and diseased hearts (Figure 2). The parameter values fitted to the simple shear experimental data (Table 1) were used as initial estimates for this fitting procedure. As shown in Figure 6, the predicted LV compliance curves for both the normal and diseased hearts did not match the corresponding experimental measurements. Accounting only for the observed

differences in LV geometry predicted that the SHR hearts would have more compliant LV chambers compared to the WKY hearts. This prediction is contrary to the experimental observations. While there may exist some issues regarding parameter identifiability, it was not possible to determine a single set of material constants that could reproduce the data from the four cases (2 WKY; 2 SHR). Therefore, it was concluded that LV hypertrophy alone could not account for the lower LV chamber compliance observed in the diseased SHR hearts.

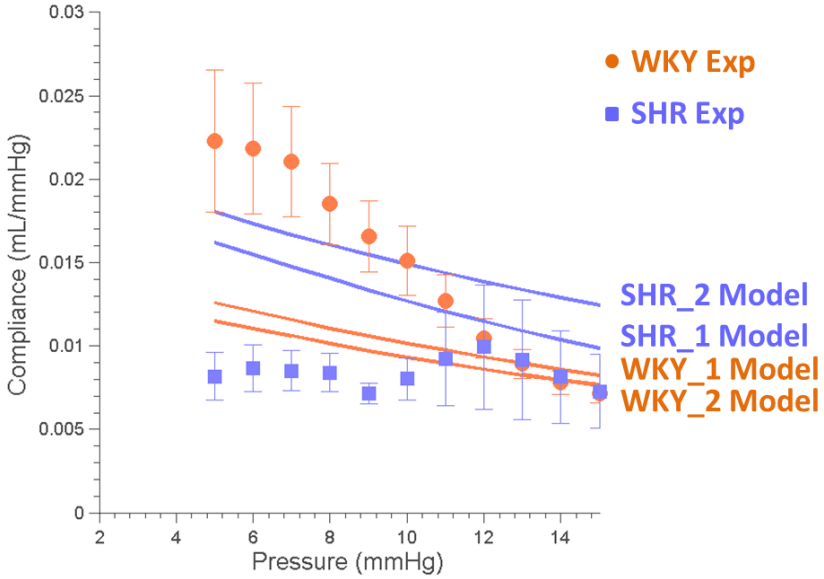

Figure 6: Experimental LV compliance curves of two normal (WKY: orange circles) and two diseased hearts (SHR: blue squares) overlaid with those predicted (WKY: orange lines; SHR: blue lines) by the FE model using original constitutive equation (Eq. 1) (Error bars indicate SD).

4.2 Hypothesis 2: LV shape changes and myocardial fibrosis explain decreased compliance

As described in Section 3.1.2, confocal imaging revealed that, in comparison to the normal WKY hearts, the diseased SHR hearts exhibited a large degree of relative thickening of the perimysial and endomysial collagen networks. By examining the high resolution confocal images of the myocardial tissue blocks (Figure 1 (b)), we estimated that the SHR myocardial endomysial collagen thickness

was approximately 5-fold greater than that in the WKY heart by visual inspection. In addition, the perimysial collagen filling the cleavage planes between sheetlets was estimated to be 10-fold thicker in the SHR hearts compared to the WKY controls. Treating the collagen thicknesses in the normal WKY myocardium as the reference (i.e. t_{endo} = 1 & t_{peri} = 1), we set the values of t_{endo} = 5 and t_{epi} = 10 for the diseased SHR hearts. With these parameters fixed, a single set of material constants were again fitted simultaneously to the experimental data using Eq. 2.

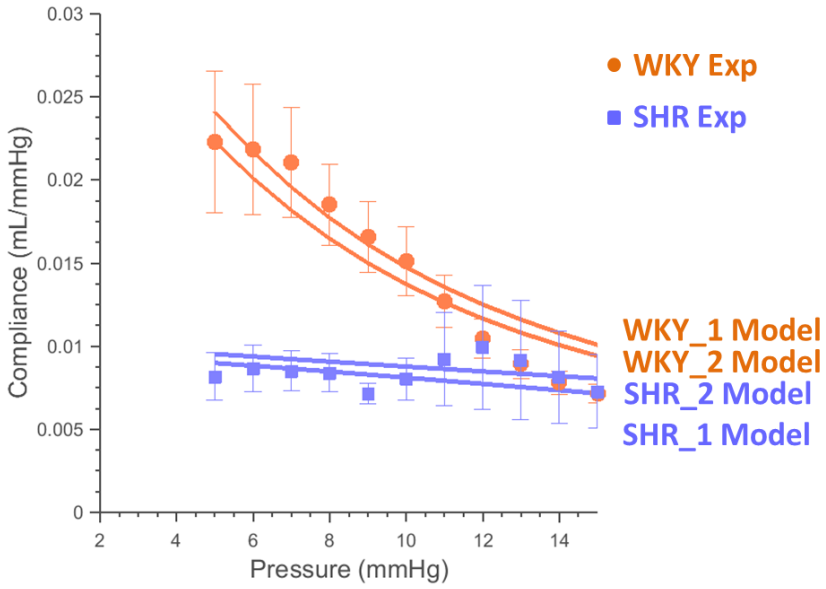

Figure 7: Experimental LV compliance curves of two normal (WKY: orange circles) and two diseased hearts (SHR: blue squares) overlaid with those predicted (WKY: orange lines; SHR: blue lines) by the FE model using the structurally modified constitutive equation (Eq. 2) (Error bars indicate SD).

Figure 7 illustrates the predicted LV compliance curves using the structurally modified constitutive equation (Eq. 2). By accounting for collagen thickening together with the LV shape changes, the LV models were able to reproduce the experimentally recorded compliance curves for both WKY and SHR hearts by fitting a single set of material constants (a_f, a_s, a_n, a_{fs}, b_f, b_s, b_n, and b_{fs}) in Eq. 2. The predicted LV compliance curves were within the inter-animal variability of the original

measurements [28] over the entire range of filling pressures for the diseased cases, and for up to 10 mmHg for the normal cases.

5 Discussion

We have developed a new constitutive modelling framework capable of assimilating information on cardiac structural and functional remodelling. We used it to investigate the underlying relationships between LV hypertrophy, myocardial fibrosis and lower chamber compliance observed in SHRs at 12-months of age compared to the WKY controls, as reported in [8].

Since many existing passive myocardial constitutive equations were not designed to incorporate knowledge on microstructural remodelling, we augmented our initial equation to include parameters that directly reflect changes in endomysial and perimysial collagen arrangement derived from the high resolution confocal microstructural images. We quantified the extent of myocardial fibrosis using two metrics: collagen volume fraction, and collagen thickening. Collagen volume fraction was not a suitable parameter with which to modify the constitutive equation, because the method of calculating collagen volume fraction was based on a fixed cross-sectional area, and this did not adequately reflect the differences in perimysial collagen proliferation and reorganisation in the diseased hearts. On the other hand, collagen thickness appeared to be a more appropriate index with which to modify the constitutive equation. Instead of using the absolute collagen thickness measurements, the structural parameters incorporated into the constitutive equation (Eq. 2) were chosen as ratios of collagen thickness normalised with respect to the age-matched WKY hearts.

The new constitutive equations (Eq. 1 and Eq. 2) developed in this study were incorporated into LV FE models to examine the relative roles of geometric remodelling and myocardial fibrosis towards elevated chamber stiffness. The increase in LV mass and LV EDV alone could not explain the

elevated chamber stiffness observed for the SHR hearts (Figure 6). However, by further accounting for the myocardial fibrosis, the normal diastolic function for the WKYs and the diastolic dysfunction for the SHRs could be reproduced (Figure 7). In each case, a single set of material parameters was identified to simultaneously fit data from the normal and diseased hearts. Therefore, the changes in organ level mechanical properties were found to be directly determined by the microstructural changes. Together with the alterations of LV gross geometry, the changes in chamber function could be completely explained. These findings are consistent with previous studies that have suggested an important role of myocardial fibrosis in diastolic dysfunction [5, 7] whereas hypertrophy is a less significant factor [5].

To our knowledge, this study was the first to produce preliminary biophysical evidence on the link between structural and functional remodelling in the heart during DHF using a model-based approach. The framework can be extended to examine SHF as well. A previous study by Eriksson et al. [35] integrated parameters that quantified the degree of fibre and sheet orientation dispersion, as has been observed in hypertrophic cardiomyopathy, into the Holzapfel-Ogden equation. By performing simulation studies of LV mechanics using a simplified model, they showed that a 10-fold increase in fibre dispersion caused a rightward shift of the LV pressure-volume loop as well as a significant increase in the end-systolic volume, which were consistent with functional changes observed in SHF. Information on the amount of sheet dispersion is rather sparse, therefore the same dispersion parameter was used for both healthy and diseased cases. Our experimental imaging protocols are well equipped to provide such information, therefore, we aim to widen our analyses to also investigate the relationship between DHF and SHF.

There are several shortcomings in the current analysis framework that require further investigation. Due to a lack of imaging data, we assumed that fibre orientations were similar for normal and diseased animals, when there may have been some remodelling of myocyte orientations. This

assumption could be addressed using *ex vivo* diffusion tensor MRI (DTMRI). It is possible to extract fibre angles for the entire heart that can be readily integrated into the LV modelling framework [36]. The *ex vivo* measurements of LV microstructure and passive function were selected from a previous study from our group using different hearts from those imaged by the *in vivo* MRI. Results from those analyses were not available for the four hearts studied here. The values of the structural parameters (t_{endo} and t_{peri}) used in this study were representative measurements derived directly from a small number of image samples. Although the model fits seemed to be more sensitive to the ways in which the constitutive equation was modified, and somewhat less sensitive to the actual values of the structural parameters, a more detailed sensitivity analysis is necessary. Better estimates of the parameters should be obtained using a larger number of microstructural images. Research is underway to develop methods to automatically quantify the degree of collagen proliferation, crimp, and reorganisation from the confocal images. Nevertheless, the proposed framework could be personalised to incorporate subject-specific *in vivo* geometry, *in vivo* mechanical function, and *ex vivo* structural parameters. Once *in vivo* imaging of collagen content (e.g. T1 mapping) becomes available, this framework could be used to provide mechanistic insights into *in vivo* heart failure mechanics on an individual-specific basis. This type of information has the potential to help clinicians with patient management and treatment options.

6 Conclusions

An image-driven constitutive modelling framework was developed and used to study the underlying mechanisms of diastolic dysfunction in SHRs. Gaining more insights into the mechanistic link between myocardial structural and functional remodelling will further our understanding of HF. The application of this approach to the analysis of *in vivo* clinical data has the potential to enable early detection of HF and more efficient treatment planning.

Acknowledgements

We gratefully acknowledge the support of the New Zealand government via funding from the Health Research Council of New Zealand, and the Marsden Fund administered by the Royal Society of New Zealand; and the financial support from the German Academic Exchange Service – DAAD for sponsoring Ms Justyna Niestrawska's Masterate thesis research at the Auckland Bioengineering Institute. We also acknowledge the valuable discussions with Prof. Bruce Smaill, and the assistance with animal experiments by Ms Linley Nisbet.

References

[1] D. L. Mann and M. R. Bristow, "Mechanisms and Models in Heart Failure: The Biomechanical Model and Beyond," *Circulation,* vol. 111, pp. 2837-2849, May 31, 2005 2005.

[2] A. M. Katz, "The "Modern" View of Heart Failure: How Did We Get Here?," *Circulation: Heart Failure,* vol. 1, pp. 63-71, May 1, 2008 2008.

[3] B. L. Leonard, B. H. Smaill, and I. J. LeGrice, "Structural Remodeling and Mechanical Function in Heart Failure," *Microscopy and Microanalysis,* vol. 18, pp. 50-67, 2012.

[4] M. Tanaka, H. Fujiwara, T. Onodera, D. Wu, Y. Hamashima, and C. Kawai, "Quantitative analysis of myocardial fibrosis in normals, hypertensive hearts, and hypertrophic cardiomyopathy," *British heart journal,* vol. 55, pp. 575-581, 1986.

[5] K. T. Weber, C. G. Brilla, and J. S. Janicki, *Myocardial fibrosis: functional significance and regulatory factors* vol. 27, 1993.

[6] B. Villari, G. Vassalli, J. Schneider, M. Chiariello, and O. M. Hess, "Age Dependency of Left Ventricular Diastolic Function in Pressure Overload Hypertrophy," *Journal of the American College of Cardiology,* vol. 29, pp. 181-186, 1// 1997.

[7] C. H. Conrad, W. W. Brooks, J. A. Hayes, S. Sen, K. G. Robinson, and O. H. L. Bing, "Myocardial Fibrosis and Stiffness With Hypertrophy and Heart Failure in the Spontaneously Hypertensive Rat," *Circulation,* vol. 91, pp. 161-170, 1995.

[8] I. J. LeGrice, A. J. Pope, G. B. Sands, G. Whalley, R. N. Doughty, and B. H. Smaill, *Progression of myocardial remodeling and mechanical dysfunction in the spontaneously hypertensive rat* vol. 303, 2012.

[9] M. A. Pfeffer, J. M. Pfeffer, and E. D. Frohlich, "Pumping ability of the hypertrophying left ventricle of the spontaneously hypertensive rat," *Circulation Research,* vol. 38, pp. 423-9, May 1, 1976 1976.

[10] O. H. Bing, C. H. Conrad, M. O. Boluyt, K. G. Robinson, and W. W. Brooks, "Studies of prevention, treatment and mechanisms of heart failure in the aging spontaneously hypertensive rat," *Heart failure reviews,* vol. 7, pp. 71-88, 2002.

[11] C. G. Brilla, L. Matsubara, and K. T. Weber, "Advanced Hypertensive Heart Disease in Spontaneously Hypertensive Rats: Lisinopril-Mediated Regression of Myocardial Fibrosis," *Hypertension,* vol. 28, pp. 269-275, August 1, 1996 1996.

[12] M. A. Rossi, "Pathologic fibrosis and connective tissue matrix in left ventricular hypertrophy due to chronic arterial hypertension in humans," *Journal of hypertension,* vol. 16, pp. 1031-1041, 1998.

[13] L. Iles, H. Pfluger, A. Phrommintikul, J. Cherayath, P. Aksit, S. N. Gupta, *et al.*, "Evaluation of Diffuse Myocardial Fibrosis in Heart Failure With Cardiac Magnetic Resonance Contrast-Enhanced T1 Mapping," *Journal of the American College of Cardiology,* vol. 52, pp. 1574-1580, 11/4/ 2008.

[14] S. Donekal, B. A. Venkatesh, Y. C. Liu, C.-Y. Liu, K. Yoneyama, C. O. Wu, *et al.*, "Interstitial Fibrosis, Left Ventricular Remodeling, and Myocardial Mechanical Behavior in a Population-Based Multiethnic Cohort: The Multi-Ethnic Study of Atherosclerosis (MESA) Study," *Circulation: Cardiovascular Imaging,* vol. 7, pp. 292-302, March 1, 2014 2014.

[15] T. P. Usyk, J. H. Omens, and A. D. McCulloch, *Regional septal dysfunction in a three-dimensional computational model of focal myofiber disarray* vol. 281, 2001.

[16] V. Wang, M. Nash, I. J. LeGrice, A. Young, B. H. Smaill, and P. J. Hunter, "Mathematical models of cardiac structure and function: mechanistic insights from models of heart failure," ed. Oxford, UK: 'Oxford University Press', 2011.

[17] J. Xi, P. Lamata, S. Niederer, S. Land, W. Shi, X. Zhuang, *et al.*, "The estimation of patient-specific cardiac diastolic functions from clinical measurements," *Medical Image Analysis,* vol. 17, pp. 133-146, 2// 2013.

[18] V. Wang, A. Young, B. Cowan, and M. Nash, "Changes in In Vivo Myocardial Tissue Properties Due to Heart Failure," in *Functional Imaging and Modeling of the Heart*. vol. 7945, S. Ourselin, D. Rueckert, and N. Smith, Eds., ed: Springer Berlin Heidelberg, 2013, pp. 216-223.

[19] D. Mojsejenko, J. McGarvey, S. Dorsey, J. Gorman, III, J. Burdick, J. Pilla, *et al.*, "Estimating passive mechanical properties in a myocardial infarction using MRI and finite element simulations," *Biomechanics and Modeling in Mechanobiology,* pp. 1-15, 2014/10/15 2014.

[20] I. J. LeGrice, B. H. Smaill, L. Z. Chai, S. G. Edgar, J. B. Gavin, and P. J. Hunter, "Laminar structure of the heart: ventricular myocyte arrangement and connective tissue architecture in the dog," *American Journal of Physiology - Heart and Circulatory Physiology,* vol. 269, pp. H571-H582, 1995.

[21] Young, Legrice, Young, and Smaill, "Extended confocal microscopy of myocardial laminae and collagen network," *Journal of Microscopy,* vol. 192, pp. 139-150, 1998.

[22] A. J. Pope, G. B. Sands, B. H. Smaill, and I. J. LeGrice, *Three-dimensional transmural organization of perimysial collagen in the heart* vol. 295, 2008.

[23] K. D. Costa, Y. Takayama, A. D. McCulloch, and J. W. Covell, *Laminar fiber architecture and three-dimensional systolic mechanics in canine ventricular myocardium* vol. 276, 1999.

[24] M. P. Nash and P. J. Hunter, "Computational Mechanics of the Heart," *Journal of elasticity and the physical science of solids,* vol. 61, pp. 113-141, 2000/07/01 2000.

[25] H. Schmid, M. P. Nash, A. A. Young, and P. J. Hunter, "Myocardial Material Parameter Estimation—A Comparative Study for Simple Shear," *Journal of Biomechanical Engineering,* vol. 128, pp. 742-750, 2006.

[26] G. A. Holzapfel and R. W. Ogden, "Constitutive modelling of passive myocardium: a structurally based framework for material characterization," *Philosophical Transactions of the Royal Society A: Mathematical, Physical and Engineering Sciences,* vol. 367, pp. 3445-3475, September 13, 2009 2009.

[27] J. D. Humphrey and F. C. P. Yin, "On Constitutive Relations and Finite Deformations of Passive Cardiac Tissue: I. A Pseudostrain-Energy Function," *Journal of Biomechanical Engineering,* vol. 109, pp. 298-304, 1987.

[28] S. Dokos, B. H. Smaill, A. A. Young, and I. J. LeGrice, *Shear properties of passive ventricular myocardium* vol. 283, 2002.

[29] Y. Lanir, "A structural theory for the homogeneous biaxial stress-strain relationships in flat collagenous tissues," *Journal of Biomechanics,* vol. 12, pp. 423-436, // 1979.

[30] A. D. Freed and T. C. Doehring, "Elastic Model for Crimped Collagen Fibrils," *Journal of Biomechanical Engineering,* vol. 127, pp. 587-593, 2005.

[31] R. Grytz and G. Meschke, "Constitutive modeling of crimped collagen fibrils in soft tissues," *Journal of the Mechanical Behavior of Biomedical Materials,* vol. 2, pp. 522-533, 10// 2009.

[32] A. A. Young, B. R. Cowan, S. F. Thrupp, W. J. Hedley, and L. J. Dell'Italia, "Left Ventricular Mass and Volume: Fast Calculation with Guide-Point Modeling on MR Images," *Radiology,* vol. 216, pp. 597-602, 2000/08/01 2000.

[33] D. D. Streeter, H. M. Spotnitz, D. P. Patel, R. John, and S. E. H., "Fiber Orientation in the Canine Left Ventricle during Diastole and Systole," *Circulation Research,* vol. 24, pp. 339-347, March 1, 1969 1969.

[34] I. J. LeGrice, B. H. Smaill, L. Z. Chai, S. G. Edgar, J. B. Gavin, and P. J. Hunter, *Laminar structure of the heart: ventricular myocyte arrangement and connective tissue architecture in the dog* vol. 269, 1995.

[35] T. S. E. Eriksson, A. J. Prassl, G. Plank, and G. A. Holzapfel, "Modeling the dispersion in electromechanically coupled myocardium," *International Journal for Numerical Methods in Biomedical Engineering,* vol. 29, pp. 1267-1284, 2013.

[36] V. Y. Wang, H. Lam, D. B. Ennis, B. R. Cowan, A. A. Young, and M. P. Nash, "Modelling passive diastolic mechanics with quantitative MRI of cardiac structure and function," *Medical image analysis,* vol. 13, pp. 773-784, 2009.

Appendix

This appendix lists some alternative structurally modified constitutive equations that failed to adequately reproduce the *ex vivo* LV compliance curves.

- Eq. A1 modulated the nonlinearity of the mechanical response with collagen thickening parameters in the sheet and sheet-normal directions only, assuming that endomysial collagen thickening had no impact on the mechanical behaviour in the fibre direction during passive inflation.

$$\bar{W} = \frac{a_f}{2b_f}\left\{\exp\left[b_f\left(I_{4f}-1\right)^2\right]-1\right\} + \frac{a_s}{2b_s}\{\exp[\boldsymbol{t_{endo}} b_s(I_{4s}-1)^2]-1\} + \frac{a_n}{2b_n}\left\{\exp\left[\boldsymbol{t_{peri}} b_n(I_{4n}-1)^2\right]-1\right\} + \frac{a_{fs}}{2b_{fs}}\left\{\exp\left[b_{fs}I_{8fs}^2\right]-1\right\} \quad \text{(A1)}$$

- Eq. A2 modified the nonlinearity of mechanical responses in all three material axes, assuming that endomysial and perimysial collagen thickening only affected the nonlinearity of the mechanical responses in all axial directions.

$$\bar{W} = \frac{a_f}{2b_f}\left\{\exp\left[\boldsymbol{t_{endo}} b_f\left(I_{4f}-1\right)^2\right]-1\right\} + \frac{a_s}{2b_s}\{\exp[\boldsymbol{t_{endo}} b_s(I_{4s}-1)^2]-1\} + \frac{a_n}{2b_n}\left\{\exp\left[\boldsymbol{t_{peri}} b_n(I_{4n}-1)^2\right]-1\right\} + \frac{a_{fs}}{2b_{fs}}\left\{\exp\left[b_{fs}I_{8fs}^2\right]-1\right\} \quad \text{(A2)}$$

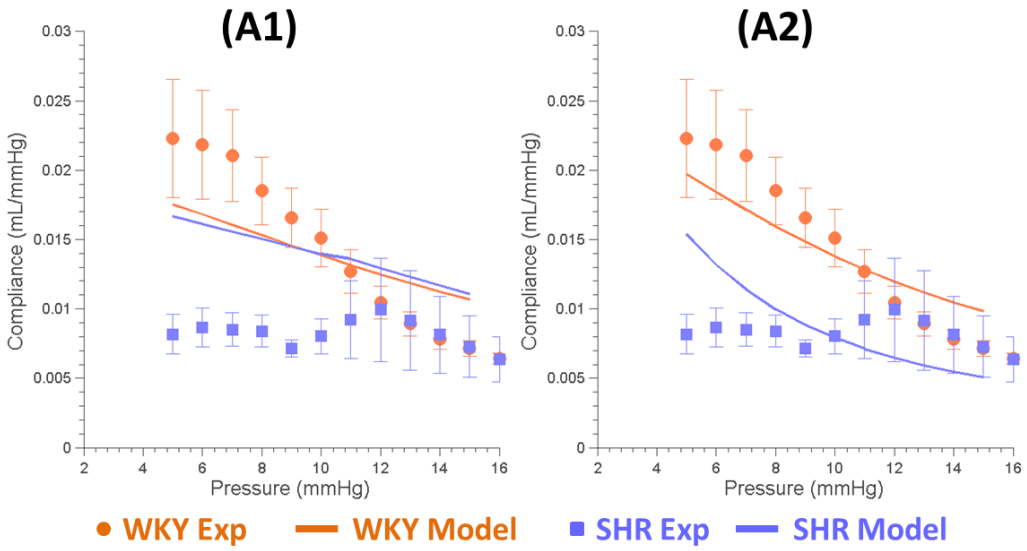

Figure 8: Experimental compliance curves for two normal (WKY: orange circles) and two diseased hearts (SHR: blue squares) overlaid with those predicted (WKY: orange lines; SHR: blue lines) by the FE model using (a) Eq. A1 and (b) Eq. A2 (Error bars indicate SD).